Controlling Solution-Phase Polymer Aggregation with Molecular Weight and Solvent Additives to Optimize Polymer-Fullerene Bulk Heterojunction Solar Cells

*Jonathan A. Bartelt, Jessica D. Douglas, William R. Mateker, Abdulrahman El Labban, Christopher J. Tassone, Michael F. Toney, Jean M. J. Fréchet, Pierre M. Beaujuge, and Michael D. McGehee**

The bulk heterojunction (BHJ) solar cell performance of many polymers depends on the polymer molecular weight (M_n) and the solvent additive(s) used for solution processing. However, the mechanism that causes these dependencies is not well understood. This work determines how M_n and solvent additives affect the performance of BHJ solar cells made with the polymer poly(di(2-ethylhexyloxy)benzo[1,2-*b*:4,5-*b*′]dithiophene-*co*-octylthieno[3,4-*c*]pyrrole-4,6-dione) (PBDTTPD). Low M_n PBDTTPD devices have exceedingly large fullerene-rich domains, which cause extensive charge-carrier recombination. Increasing the M_n of PBDTTPD decreases the size of these domains and significantly improves device performance. PBDTTPD aggregation in solution affects the size of the fullerene-rich domains and this effect is linked to the dependency of PBDTTPD solubility on M_n. Due to its poor solubility high M_n PBDTTPD quickly forms a fibrillar polymer network during spin-casting and this network acts as a template that prevents large-scale phase separation. Furthermore, processing low M_n PBDTTPD devices with a solvent additive improves device performance by inducing polymer aggregation in solution and preventing large fullerene-rich domains from forming. These findings highlight that polymer aggregation in solution plays a significant role in determining the morphology and performance of BHJ solar cells.

1. Introduction

The certified power conversion efficiencies (PCE) of polymer-fullerene bulk heterojunction (BHJ) solar cells[1] are now above 9 and 10% in single-junction[2] and tandem[3] architectures, respectively. Much of the recent improvement in device performance is due to the design and synthesis of new donor-acceptor (D-A) polymers that have energy levels and band gaps optimized for high PCE.[4–9] Designing new D-A polymers is a formidable task because it is difficult to predict if a given D-A chemical structure will yield high BHJ solar cell performance.[10] Furthermore, optimizing the photovoltaic performance of a new polymer is complex because the process involves not only controlling the regioregularity, polydispersity, and molecular weight of the polymer during synthesis, but also tuning the morphology of the polymer-fullerene BHJ during thin-film processing in order to obtain the best performance.[11,12]

For a variety of D-A polymers, it has been reported that there is a correlation between the number-average molecular weight (M_n) of the polymer and its BHJ solar cell performance.[13–26] In some cases this correlation is quite strong, with device PCE increasing by ≈100% when the M_n of the polymer is increased from ≈15 to ≈30 kDa.[13,20,21] Modest differences in M_n can thus lead to significant batch-to-batch variations and differences in the performance of the same polymer when synthesized by different research groups.[27–30] Previous studies have examined the effects of M_n on D-A polymer photoresponsivity,[17] molecular orientation,[20] hole mobility,[21] and fibrillar structure.[26] However, a complete model that predicts how differences in M_n cause the observed morphological and photophysical changes, and describes why these changes affect device performance, has not yet been developed.

To optimize the morphology of D-A polymer-based BHJs, high-boiling-point solvent additives are often used during solution processing.[21,31–45] Studies on many D-A polymer-fullerene systems have shown that solvent additives inhibit

J. A. Bartelt, W. R. Mateker, Prof. M. D. McGehee
Department of Materials Science and Engineering
Stanford University
Stanford, CA, 94305, USA
E-mail: mmcgehee@stanford.edu
Dr. J. D. Douglas, Prof. J. M. J. Fréchet
Department of Chemistry
University of California
Berkeley, CA, 94720, USA
Dr. A. El Labban, Prof. J. M. J. Fréchet, Prof. P. M. Beaujuge
Physical Sciences and Engineering Division
King Abdullah University of Science and Technology
Thuwal, 23955–6900, Saudi Arabia
Dr. C. J. Tassone, Dr. M. F. Toney
Stanford Synchrotron Radiation Lightsource
SLAC National Accelerator Laboratory
Menlo Park, CA, 94025, USA

DOI: 10.1002/aenm.201301733

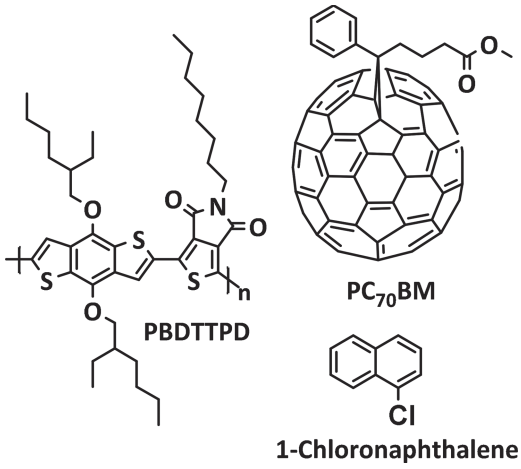

Figure 1. Chemical structures of PBDTTPD, $PC_{70}BM$, and 1-chloronaphthalene.

large-scale phase separation and prevent the formation of large fullerene-rich domains.[21,36–40,43,45] While these studies have characterized the morphological changes induced by solvent additives, researchers have only recently begun to study the underlying mechanism that leads to these morphological changes.[46] Furthermore, there is still a lack of understanding in how said morphological changes affect device performance.

In this report, we examine how the polymer M_n and the use of the solvent additive, 1-chloronaphthalene (CN), affect the performance of BHJ solar cells based on the D-A polymer poly(di(2-ethylhexyloxy)benzo[1,2-*b*:4,5-*b'*]dithiophene-*co*-octylthieno[3,4-*c*]pyrrole-4,6-dione) (PBDTTPD)[27–29] and [6,6]-phenyl-C_{70}-butyric acid methyl ester ($PC_{70}BM$) (**Figure 1**). The PCE of PBDTTPD devices made without CN strongly depends on M_n, and processing these BHJs with CN preferentially improves the performance of low M_n PBDTTPD devices. Using X-ray diffraction and transmission electron microscopy, we show that differences in BHJ morphology cause the dependency of device performance on M_n and the use of CN. With ultraviolet-visible spectroscopy and X-ray scattering techniques, we examine the morphology of PBDTTPD in solution and develop a model that describes why the polymer M_n affects the performance of these devices. In this model, PBDTTPD aggregation in solution plays a primary role in determining the BHJ morphology, and we infer that this effect is largely caused by the dependency of PBDTTPD solubility on M_n. In parallel, we infer that CN affects device performance by altering the relative solubilities of PBDTTPD and $PC_{70}BM$ in solution such that low M_n PBDTTPD aggregates extensively in solution while $PC_{70}BM$ is still solubilized. Lastly, using a combination of light-intensity-dependent and bias-dependent quantum efficiency measurements, we elucidate how and why the morphology of low M_n PBDTTPD BHJs hinders photovoltaic performance.

2. Results and Discussion

2.1. Performance of PBDTTPD:$PC_{70}BM$ BHJ Solar Cells

Herein, we examine the BHJ solar cell performance and morphology of four batches of PBDTTPD with M_n of 23, 29, 36, and 39 kDa and polydispersity indexes (PDIs) of 1.6, 1.8, 1.8, and 1.8, respectively. All devices were fabricated with PBDTTPD and $PC_{70}BM$ in a 1:1.5 weight ratio, and were either spin-cast from chlorobenzene (CB) or a 95/5 (by volume) mixture of CB and CN. Devices made with 39 kDa PBDTTPD and processed in CB yield an average PCE of 7.4%, open-circuit voltage (V_{OC}) of 0.94 V, and fill factor (FF) of 0.71 (**Table 1** and **Figure 2**a). The 36, 29, and 23 kDa PBDTTPD batches show significantly lower device PCEs of 5.9, 4.6, and 3.4%, respectively. These

Table 1. Figures of merit for PBDTTPD:$PC_{70}BM$ BHJ solar cells. Average values and standard deviations are calculated from at least 25 devices.

M_n [kDa]	CN [vol%]	J_{SC} [mA cm^{-2}]	V_{OC} [V]	FF	PCE [%]	PCE improvement with CN [%]
39	0	11.2 ± 0.5	0.94 ± 0.01	0.71 ± 0.01	7.4 ± 0.3	–
	5	12.5 ± 0.3	0.95 ± 0.01	0.70 ± 0.02	8.3 ± 0.3	12
36	0	9.3 ± 0.4	0.97 ± 0.01	0.65 ± 0.01	5.9 ± 0.3	–
	5	11.9 ± 0.4	0.94 ± 0.01	0.67 ± 0.02	7.4 ± 0.2	25
29	0	7.8 ± 0.4	0.98 ± 0.01	0.60 ± 0.01	4.6 ± 0.2	–
	5	11.4 ± 0.5	0.94 ± 0.01	0.67 ± 0.02	7.2 ± 0.3	57
23	0	6.2 ± 0.3	0.97 ± 0.01	0.56 ± 0.01	3.4 ± 0.2	–
	5	10.0 ± 0.3	0.94 ± 0.01	0.59 ± 0.01	5.5 ± 0.2	62

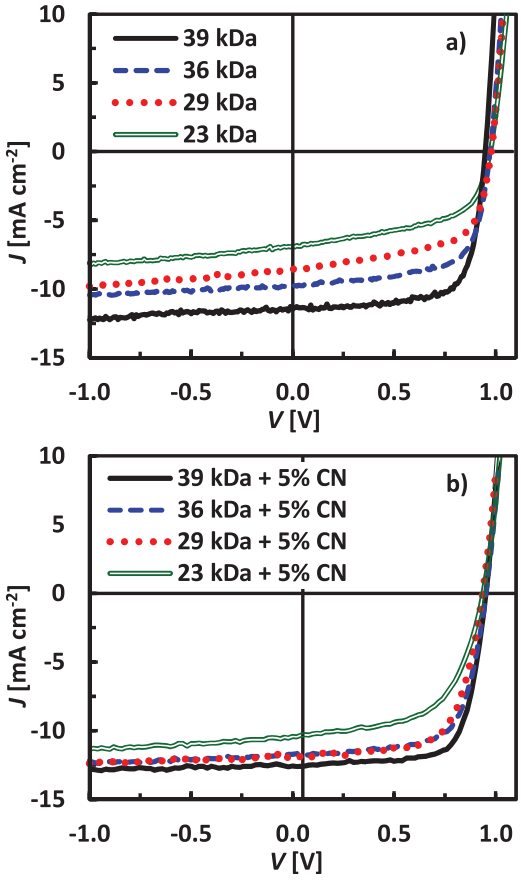

Figure 2. Current density–voltage (*J*–*V*) characteristics for PBDTTPD BHJ solar cells processed a) in chlorobenzene and b) in a 95/5 (by volume) mixture of chlorobenzene and 1-chloronaphthalene.

lower PCE values are due to substantial decreases in both the device short-circuit current (J_{SC}) and FF. The strong correlation between device J_{SC} and FF and M_n has been previously reported for a variety of D-A polymer-fullerene systems,[13,26] and while authors often do not report the results of M_n optimizations, it is generally the case that the best device performance is obtained with high M_n polymers. A variety of other research groups have studied PBDTTPD BHJ solar cells and reported average PCEs of 2.7,[23] 4.2,[28] 5.5,[29] 6.3,[27] and 7.1%[47] for devices processed without solvent additives. We hypothesize that differences in M_n likely contribute to these large variations in reported PCEs since relatively small changes in M_n (23 to 39 kDa) lead to significant differences in device PCE (3.4 to 7.4%).

Processing PBDTTPD BHJs in a mixture of CB and CN, instead of CB alone, has previously been shown to improve the performance of PBDTTPD BHJ solar cells.[23,30] We find that the PCE of low M_n PBDTTPD devices is particularly improved by incorporating CN, as the PCE of 23 and 29 kDa devices increases from 3.4 to 5.5% (an improvement of ≈62%) and 4.6 to 7.2% (an improvement of ≈57%), respectively. Processing with CN, however, improves the PCE of 36 and 39 kDa devices less drastically from 5.9 to 7.4% (an improvement of ≈25%) and from 7.4 to 8.3% (an improvement of ≈12%), respectively. These improvements in PCE are due to increases in both the device J_{SC} and FF (Table 1 and Figure 2b). High M_n PBDTTPD devices processed with CN perform remarkably well and their high V_{OC} (0.95 V) and FF (0.70) make PBDTTPD an excellent candidate for the high-bandgap subcell in a tandem solar cell.[3,48,49]

2.2. Effects of PBDTTPD M_n on Thin-Film Morphology

The PBDTTPD chemical structure, fullerene chemical structure, and device architecture were held constant for all the solar cells made in this study, so morphological aspects likely govern the performance of the devices made with PBDTTPD of various M_n. Using bright-field transmission electron microscopy (TEM), we find that the large-scale morphology of PBDTTPD BHJs processed in CB changes drastically when the M_n is increased from 23 to 39 kDa (**Figure 3**, top row). In 23 kDa PBDTTPD BHJs, ≈300–400 nm diameter dark-colored domains are clearly visible, and when the M_n is increased to 29 kDa, the diameter of these domains decreases to ≈100–200 nm. Large domains like these have been observed in other D-A polymer BHJs and are generally identified as fullerene-rich domains because fullerenes have a higher electron density than most D-A polymers and scatter electrons more strongly.[36–38,40] Thus, we infer that the large, dark-colored domains in low M_n PBDTTPD BHJs processed in CB are $PC_{70}BM$-rich domains. In the 36 and 39 kDa PBDTTPD BHJs, large, dark-colored domains are not easily discernible. This observation suggests that either the contrast between the $PC_{70}BM$-rich domains and the surrounding polymer-rich matrix is decreased in these BHJs (because the PBDTTPD and $PC_{70}BM$ are more mixed), or the $PC_{70}BM$-rich domains in these BHJs are small enough for multiple domains to overlap throughout the thickness of the thin-film. Thus, increasing the M_n of PBDTTPD prevents ≈300–400 nm $PC_{70}BM$-rich domains from forming in these BHJs. One can also discern small, light-colored, fibrillar

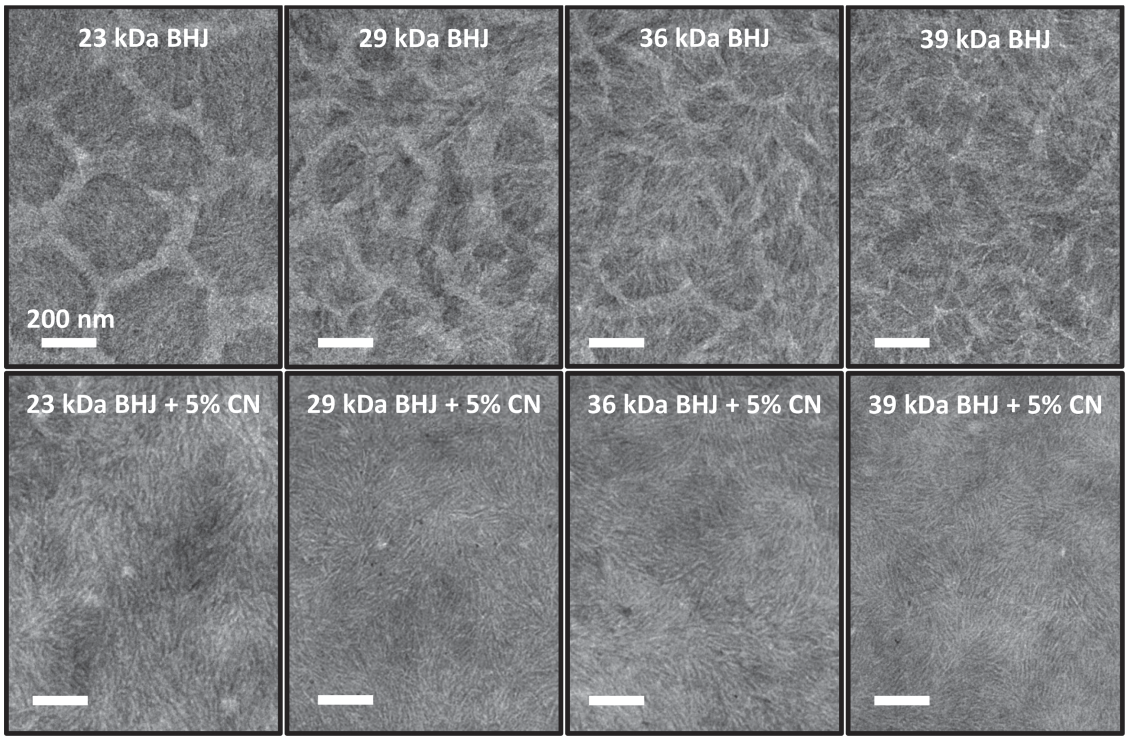

Figure 3. Top-down bright-field TEM images of PBDTTPD BHJs. Top row: processed in chlorobenzene. Bottom row: processed in a 95/5 (by volume) mixture of chlorobenzene and 1-chloronaphthalene. The scale bar is 200 nm in all of the images.

features in the TEM images of the 36 and 39 kDa PBDTTPD BHJs. These fibrillar features are likely PBDTTPD fibrils, which have been observed before in PBDTTPD:$PC_{60}BM$ BHJs.[50] In the 29 kDa PBDTTPD BHJ, these fibrillar features are much more difficult to discern, and in the 23 kDa PBDTTPD BHJ there are no discernible fibrillar features. This observation suggests that the propensity of PBDTTPD to form fibrils in these BHJs increases with M_n.

We find that processing PBDTTPD BHJs with a mixture of CB and CN prevents the formation of large $PC_{70}BM$-rich domains and increases the size of the PBDTTPD fibrils in all samples (Figure 3, bottom row). There are well-defined, light-colored fibrillar features in the 23, 29, 36, and 39 kDa PBDTTPD BHJs processed with CN and the domain sizes in each of these BHJs are near-equivalent. These findings are similar to previous reports, which have shown that solvent additives prevent the formation of large fullerene-rich domains[21,36–40,43,45] and increase the degree of polymer order in D-A polymer BHJ thin-films.[36,41,42]

It has been proposed that polymer crystallization drives phase separation and the formation of fullerene-rich domains in poly(3-hexylthiophene) (P3HT)-fullerene BHJs.[51,52] Because fullerenes only mix with the amorphous portions of semicrystalline P3HT,[53,54] P3HT crystallization expels fullerene into the amorphous regions of the polymer, increases the fullerene concentration in these regions, and eventually initiates fullerene phase separation. To determine if extensive PBDTTPD crystallization causes the large-scale fullerene phase separation in low M_n PBDTTPD BHJs, we examined the degree of polymer order in PBDTTPD BHJ thin-films with grazing incidence X-ray diffraction (GIXD). Regardless of M_n, the width of the PBDTTPD diffraction peaks in the GIXD images of both neat polymer and BHJ thin-films is quite broad, indicating that the diffraction in these thin-films is from poorly ordered polymer domains rather than well-ordered nanofibers like those formed by low M_n P3HT[55] (Figure S1–S4, Supporting Information). To quantitatively compare the degree of aggregation (here we define an "aggregate" as a group of π-stacked polymer backbones[56]) in PBDTTPD thin-films as a function of M_n, we constructed pole figures for the π–π stacking diffraction peak using the method described by Baker et al. (**Figure 4**).[57] These pole figures plot the π–π stacking diffraction intensity as a function of the angle, χ, between the π–π stacking direction and the substrate normal. The relative degree of aggregation (*rDoA*) is compared between samples using Equation (1), which integrates the GIXD intensity in the pole figure, $I(\chi)$, across all orientations (with a $\sin(\chi)$ geometrical correction factor).[58]

$$rDoA \propto \int_0^{\pi/2} \sin(\chi) I(\chi) \mathrm{d}\chi \quad (1)$$

We find that the *rDoA* increases by ≈35% ± 14% (the error is primarily due to uncertainty in the measured sample volume) in neat PBDTTPD thin-films processed in CB when the M_n is increased from 23 to 39 kDa (Table S1, Supporting Information). Furthermore, processing with CN increases the *rDoA* of both 23 and 39 kDa neat PBDTTPD thin-films by ≈74% ± 14% and ≈23% ± 14%, respectively. Pole figures of the PBDTTPD π–π stacking in BHJ thin-films reveal similar trends, although

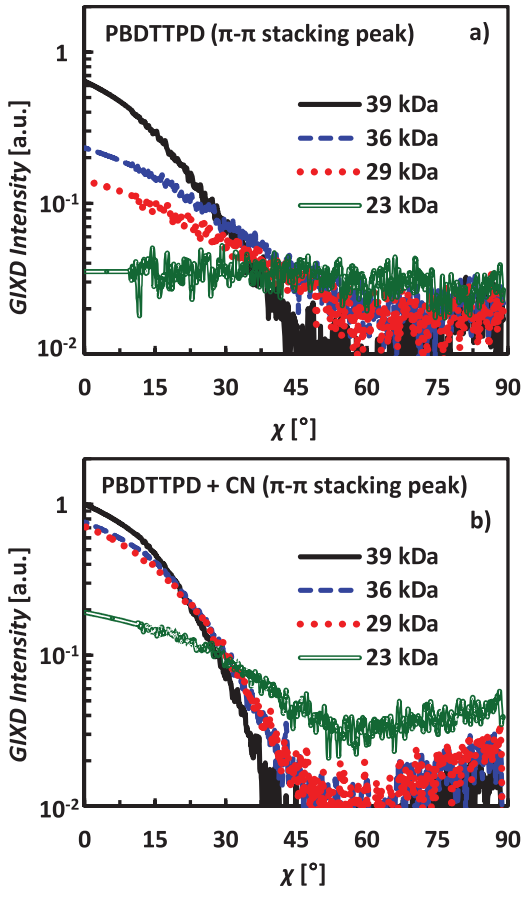

Figure 4. Complete pole figure for the π–π stacking diffraction peak ($q \approx 1.7$ Å^{-1}) for neat PBDTTPD thin-films processed a) in chlorobenzene and b) in a 95/5 (by volume) mixture of chlorobenzene and 1-chloronaphthalene. All data is normalized by the grazing incidence X-ray diffraction intensity of the 39 kDa CN sample at $\chi = 0°$.

quantitative analysis of the diffraction intensity is more difficult due to the presence of additional X-ray scattering peaks from amorphous $PC_{70}BM$ clusters (Figure S5, Supporting Information). Thus, the two conditions that deter the formation of large $PC_{70}BM$-rich domains in PBDTTPD BHJs, use of high M_n polymer and use of CN, both increase the degree of PBDTTPD aggregation. Based on these results, we infer that low M_n PBDTTPD is not highly ordered and conclude that the large-scale $PC_{70}BM$ phase separation in low M_n PBDTTPD BHJs is not caused by there being a lack of amorphous PBDTTPD with which the $PC_{70}BM$ can mix.

Pole figures also provide information about the distribution of angular orientations (texture) of the PBDTTPD aggregates. In both neat polymer (Figure 4) and BHJ thin-films (Figure S5, Supporting Information), the fraction of PBDTTPD aggregates with "face-on" orientations (π–π stacking out-of-plane, $\chi \approx 0°$) increases as the M_n is increased. Additionally, processing films with CN increases the fraction of aggregates with "face-on" orientations compared to the thin-films processed in CB alone, for all M_n. The presence of these "face-on" oriented aggregates may improve hole transport in solar cells made with high M_n PBDTTPD and those processed with CN.[46,59]

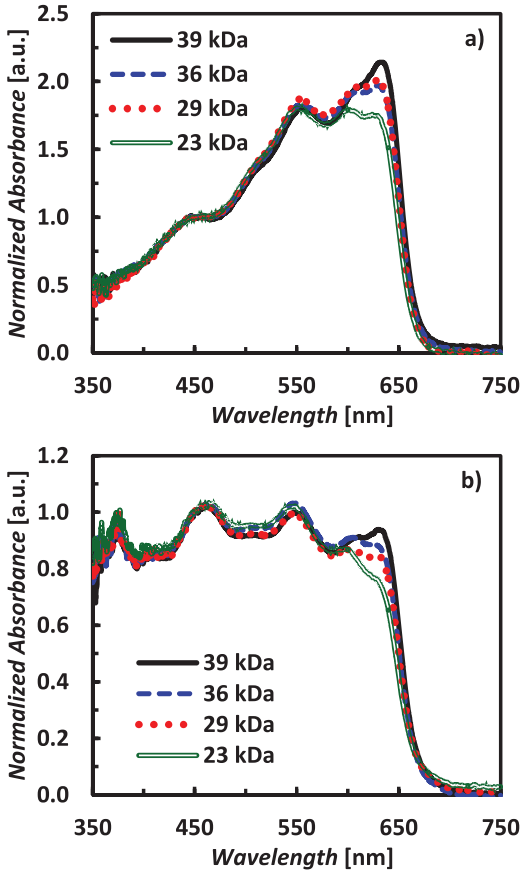

Figure 5. Absorbance vs. wavelength for a) PBDTTPD and b) PBDTTPD:$PC_{70}BM$ (1:1.5 by weight) solutions in chlorobenzene (≈0.1 mg PBDTTPD mL^{-1}) at ≈25 °C. The spectra are normalized to the absorbance at 450 nm.

2.3. Morphology of PBDTTPD in Solution

We hypothesize that the relatively high degree of aggregation in high M_n PBDTTPD thin-films and PBDTTPD thin-films processed with CN arises from an increased propensity of the polymer in these samples to aggregate in solution. To characterize the morphology of PBDTTPD in solution, we examined the absorption characteristics of dilute PBDTTPD solutions with ultraviolet-visible (UV-Vis) spectroscopy. Independent of M_n, the absorption spectra of the PBDTTPD solutions have peaks at ≈450, ≈500, ≈550, ≈600, and ≈625 nm (**Figure 5**). The absorption features at 450, 500, 550, 600 nm are relatively unaffected by the solution temperature and M_n (Figure S6–S9, Supporting Information). The strength of the red-shifted absorption feature at 625 nm, however, decreases significantly in both neat PBDTTPD and PBDTTPD:$PC_{70}BM$ solutions when the solution temperature is increased from ≈25 to ≈115 °C. Steyrleuthner et al.[60] studied the aggregation of the D-A polymer P(NDI2OD-T2) in solution and found that increasing the solution temperature decreased the fraction of P(NDI2OD-T2) chains that were aggregated. Furthermore, the authors determined that the P(NDI2OD-T2) aggregate absorption features were red-shifted because the polymer chains within the aggregates adopted planar conformations. Based on these findings, we attribute the absorption feature at ≈625 nm in PBDTTPD solutions to the absorption of a PBDTTPD aggregate species. The strength of this red-shifted absorption feature increases in both neat PBDTTPD and PBDTTPD:$PC_{70}BM$ solutions when the M_n of PBDTTPD is increased. This finding suggests that the fraction of PBDTTPD chains that are aggregated in solution increases as the M_n is increased.

UV-vis absorption experiments were performed on dilute PBDTTPD solutions (≈0.1 mg PBDTTPD mL^{-1}) because the absorbance of the concentrated solutions (≈8 mg PBDTTPD mL^{-1}) used to spin-cast solar cells is exceedingly high. To probe the morphology of PBDTTPD in concentrated solutions, we used a combination of small-angle X-ray scattering (SAXS) and ultra-small-angle X-ray scattering (USAXS) experiments. The solutions were held at ≈70 °C (the highest temperature attainable with our experimental setup) during these scattering experiments to better probe the polymer morphology in the heated solutions used to spin-cast solar cells. The combined SAXS and USAXS data was analyzed using the unified approach, which combines Porod's and Guinier's laws.[61–63] With this approach, the radius of gyration (R_g) can be determined, which is a measure of the total effective size of both the structures that form in solution as well as the sub-unit building blocks of these structures. Furthermore, the Porod scaling, which provides information about the fractal dimension of the structures as well as the geometry of the sub-units within the structures, can be elucidated.[64,65]

Several similarities are found when comparing the combined SAXS and USAXS scattering profiles of the 23, 29, 36, and 41[66] kDa PBDTTPD solutions (**Figure 6**). We find that all the solutions have Guinier regions in both the low q vector ($q < 0.001$ $Å^{-1}$) and high q vector ($q > 0.1$ $Å^{-1}$) regions. Using the Guinier model, we fit the shoulder in the low q region and attribute this scattering to large multi-chain PBDTTPD agglomerates (here we define an "agglomerate" as an ensemble of many loosely connected polymer chains, in which there is not necessarily ordered π–π or lamellar stacking) with R_g in excess of 300 nm (a lower limit since the full extent of the plateau is not resolved). At high q vectors, fitting the Guinier region provides a R_g of ≈6.3 Å, independent of M_n, which indicates that this scattering feature likely arises from the fundamental building block of the PBDTTPD agglomerates, the polymer repeat unit.

Further evaluation of the scattering profiles reveals two Porod regimes with distinctly different power law dependencies. In the first Porod region, corresponding to ≈0.0008 $Å^{-1} < q <$ ≈0.006 $Å^{-1}$, the 23, 29 and 41 kDa PBDTTPD solutions have a Porod scaling of $q^{-2.7}$, while the 36 kDa solution has a Porod scaling of $q^{-2.9}$. A Porod scaling near q^{-3} indicates that the PBDTTPD chains that make up the large multi-chain agglomerates are in collapsed coil conformations rather than Gaussian coil or expanded coil conformations (Porod scaling of q^{-2} and $q^{-5/3}$, respectively).[64] In the second Porod region at q vectors between ≈0.015 and ≈0.1 $Å^{-1}$, the Porod scaling changes to q^{-1} for each solution, which indicates that at shorter length scales (≈20 nm) there is scattering from PBDTTPD backbones with stiff, rod-like conformations.[67] Taken together, these findings indicate that at 70 °C all the solutions, independent of M_n, contain large agglomerates composed of loosely-connected PBDTTPD chains in collapsed coil conformations, and within

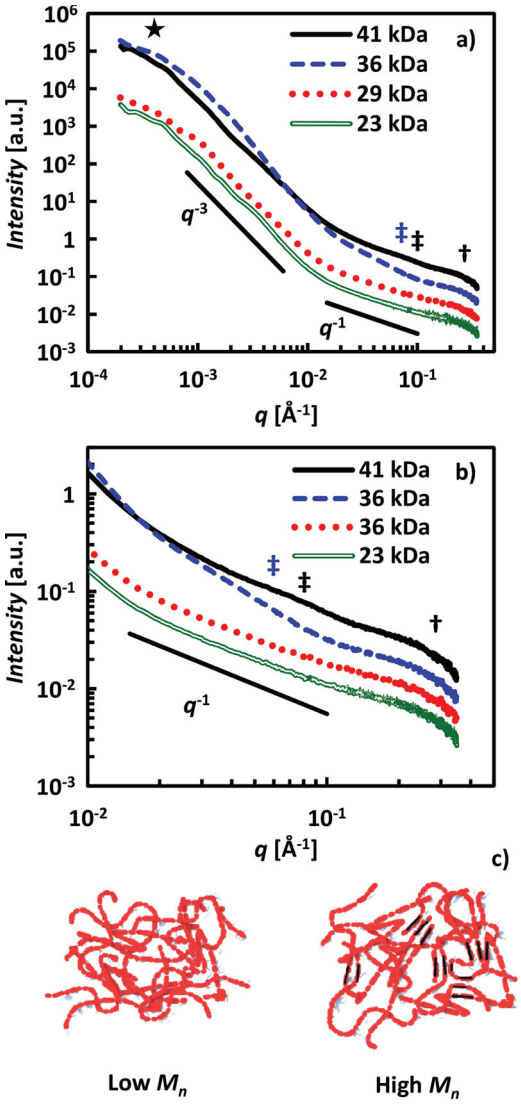

Figure 6. a) Combined ultra-small angle X-ray scattering and small-angle X-ray scattering intensity vs. q for PBDTTPD dissolved in chlorobenzene (≈8 mg PBDTTPD mL^{-1}) at 70 °C. The low q vector Guinier region is marked by a star and the high q vector Guinier region is marked by a dagger. The solid black lines indicate the slope change in the Porod scaling as it moves from $q^{-2.7}$ to q^{-1}. The intermediate Guinier region is marked by blue and black double daggers for the 36 and 41[66] kDa solutions, respectively. b) Plot showing the same data as in (a), but zoomed-in on the intermediate Guinier regime. c) Proposed morphologies of low and high M_n PBDTTPD agglomerates in solution. High M_n PBDTTPD agglomerates have small ordered building blocks, which are not present in low M_n PBDTTPD agglomerates.

these agglomerates there are regions where the polymer backbones are stiff and rod-like.

While the scattering profiles of the four PBDTTPD solutions are largely similar, there is a subtle difference between the scattering observed from the low and high M_n PBDTTPD solutions. The high M_n solutions have an intermediate Guinier regime (marked by double daggers in Figure 6) that corresponds to R_g values of ≈5.3 and ≈2.6 nm for the 36 and 41 kDa solutions, respectively. This intermediate Guinier regime, which is not present in the 23 and 29 kDa solutions, likely arises from a second building block, in addition to the polymer repeat unit, within the agglomerate. We hypothesize that these secondary building blocks consist of several monomer repeat units coupled into ordered structures. A schematic comparing the proposed morphologies of low and high M_n PBDTTPD agglomerates is shown in Figure 6. We suspect that this difference in agglomerate morphology arises because of differences in polymer solubility. Generally, the solubility of a polymer in a solvent decreases as the M_n is increased because the entropy of mixing (per unit volume) of the polymer solution decreases when the length of the polymer molecules is increased.[68] As a result, high M_n PBDTTPD likely has the strongest propensity to self-assemble in solution.

2.4. Fibrillar Network Templates Phase Separation

Russell et al.[42,43] proposed that some solvent additives function by promoting the formation of polymer aggregates in solution. It was hypothesized that these aggregates coalesce and form a fibrillar network during the film drying process, and this network sets the characteristic length scale for phase separation in the BHJ. We hypothesize that a similar mechanism controls the domain size in PBDTTPD BHJs. Early in the spin-casting process, high M_n PBDTTPD, because of its low solubility, forms large multi-chain agglomerates that are composed of somewhat-ordered secondary (smaller) building block structures. These secondary building block structures may act as distributed seed sites, which initiate PBDTTPD aggregation and facilitate the formation of polymer fibrils in solution. This process may lead to the rapid formation of a fibrillar PBDTTPD network during spin-casting as the solution concentration increases and the solution temperature decreases. Since high M_n PBDTTPD is less soluble than $PC_{70}BM$, the PBDTTPD fibrillar network is formed while the $PC_{70}BM$ is still solubilized. Once formed, this PBDTTPD network may function as a template that defines the maximum domain size that can be formed when PBDTTPD and $PC_{70}BM$ phase separate. Thus, by forming a fibrillar network before the onset of large-scale phase separation, the polymer is able to control the size of the $PC_{70}BM$-rich domains. In contrast, low M_n PBDTTPD may not form a fibrillar network quickly enough during the spin-casting process to prevent large-scale phase separation. In low M_n PBDTTPD solutions, the only building block that makes up the large multi-chain agglomerates is the polymer repeat unit. As a result, there are few seed sites that can initiate PBDTTPD aggregation and fibril formation in solution. Thus, we believe the dependency of morphology on the M_n of PBDTTPD is largely related to the polymer solubility and the propensity of high M_n PBDTTPD to self-assemble in solution.

We infer that CN prevents the formation of large $PC_{70}BM$-rich domains in low M_n PBDTTPD devices via a similar mechanism. When spin-casting PBDTTPD BHJs from a heated mixture of CB and CN, the majority of the CB quickly evaporates and leaves a CN-saturated solution of PBDTTPD and $PC_{70}BM$ behind.[69] The solubility of $PC_{70}BM$ is as high as 400 mg mL^{-1} in CN at room temperature, which is significantly higher than the solubility of typical D-A polymers in CN (<100 mg mL^{-1}).[35]

Thus, in a CN-saturated solution both low and high M_n PBDTTPD likely crash out of solution and form a fibrillar network while the $PC_{70}BM$ is still solubilized. This polymer network, as discussed previously, may act as a template for phase separation and limit the $PC_{70}BM$-rich domain size.

It should be noted that not all D-A polymer-fullerene systems undergo large-scale phase separation when spin-cast without solvent additives. Some D-A polymer-fullerene systems form a finely intermixed morphology and require the use of solvent additives to increase the degree of phase separation in order to achieve optimal solar cell performance.[31,41,70] Determining why certain polymer-fullerene systems mix well and others readily phase separate when spin-cast is beyond the scope of this study, but polymer aggregation in solution is likely applicable in both situations. In polymer-fullerene systems that form finely intermixed morphologies, solvent additives may induce polymer aggregation in solution and increase the degree of phase separation in the BHJ. On the other hand, in polymer-fullerene systems that readily phase separate, such as the PBDTTPD:$PC_{70}BM$ system, solvent additives can control fullerene phase separation by promoting polymer aggregation in solution while the fullerene is still solubilized, which prevents large-scale phase separation.[46]

2.5. Loss Mechanisms in Low M_n PBDTTPD Devices

Photocurrent generation in polymer-fullerene BHJ solar cells is thought to occur via four processes: i) absorption of a photon by either the polymer or fullerene, which forms an exciton, ii) dissociation of the exciton at a polymer-fullerene heterojunction forming a charge-transfer state, iii) separation of the charge-transfer state into a free electron and hole, and iv) extraction of the free charge-carriers from the device. Inefficiency in any one (or combination) of these processes reduces the quantum efficiency of a given device. In order to determine how the M_n of PBDTTPD affects the efficiency of these processes, we examined the device characteristics of PBDTTPD BHJ solar cells.

We find that decreasing the M_n of PBDTTPD lowers the external quantum efficiency (EQE) of PBDTTPD devices across all wavelengths, from a spectrally-averaged ≈63% for 39 kDa PBDTTPD to ≈54, ≈48, and ≈41% for 36, 29, and 23 kDa PBDTTPD, respectively (Figure S10a). When devices are processed in CN, which prevents large $PC_{70}BM$-domain growth, the EQE is enhanced across all wavelengths with the largest improvement in low M_n PBDTTPD devices (Figure S10b). This finding indicates that the morphology of low M_n devices limits the efficiency of photocurrent generation in the regions of the solar spectrum where both PBDTTPD and $PC_{70}BM$ absorb photons. The EQE, however, is a product of the efficiency of each of the aforementioned processes involved in photocurrent generation, so additional analyses are needed to elucidate which specific processes are affected by the morphology of low M_n PBDTTPD BHJs.

We measured the internal quantum efficiency (IQE) of PBDTTPD BHJ solar cells to determine if differences in light absorption account for the reduced EQE and J_{SC} of low M_n devices (**Figure 7**). The IQE of PBDTTPD devices decreases significantly across all wavelengths as the M_n is reduced, from

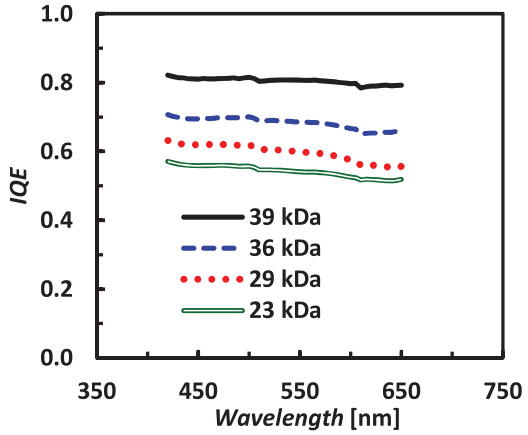

Figure 7. Internal quantum efficiency vs. wavelength for PBDTTPD BHJ solar cells processed in chlorobenzene.

a spectrally-averaged ≈81% for 39 kDa PBDTTPD to ≈69, ≈60, and ≈55% for 36, 29, and 23 kDa PBDTTPD, respectively. This result verifies that the performance of low M_n PBDTTPD devices is limited by inefficient excitonic and/or electronic processes rather than by optical losses.

To probe the efficiency of exciton harvesting in PBDTTPD BHJs, we performed steady-state photoluminescence (PL) measurements on neat polymer and BHJ films (Figure S11 and Table S2, Supporting Information). We find that >98% of the emissive PBDTTPD excitons are quenched in PBDTTPD BHJs, regardless of M_n, which suggests that the majority of excitons generated (with an excitation wavelength of 515 nm) in these BHJs are able to reach PBDTTPD-PCBM heterojunction interfaces. We note that steady-state PL measurements do not probe the majority of polymer excitons, which decay non-radiatively. However, the PL quenching efficiency in P3HT BHJs determined via steady-state PL measurements was shown to agree with the P3HT exciton harvesting efficiency obtained from a detailed analysis of the IQE of P3HT BHJ solar cells.[71] Steady-state PL measurements also only probe a small fraction of the $PC_{70}BM$ excitons because the PL quantum efficiency of fullerenes is exceedingly low.[72] But, if poor $PC_{70}BM$ exciton harvesting efficiency was the primary factor limiting the IQE of low M_n PBDTTPD devices, one would expect the IQE of these devices to preferentially decrease in the blue region of the solar spectrum, where $PC_{70}BM$ is the stronger absorber. However, the IQE of PBDTTPD devices decreases across all wavelengths as the M_n is decreased, which indicates that inefficient exciton harvesting is likely not significantly limiting the IQE of low M_n PBDTTPD devices.

The rate of bimolecular recombination in a BHJ solar cell is proportional to the product of the electron and hole densities in the device. Thus, one can probe the amount of recombination loss due to bimolecular recombination in PBDTTPD devices using light-intensity-dependent IQE measurements (**Figure 8**a). For these measurements, devices are irradiated with a low intensity, optically-chopped monochromatic light, which is superimposed over a white-light bias. The differential IQE, ΔIQE, of the solar cell at J_{SC} is then measured with a lock-in amplifier while the intensity of the white-light bias is varied.[73]

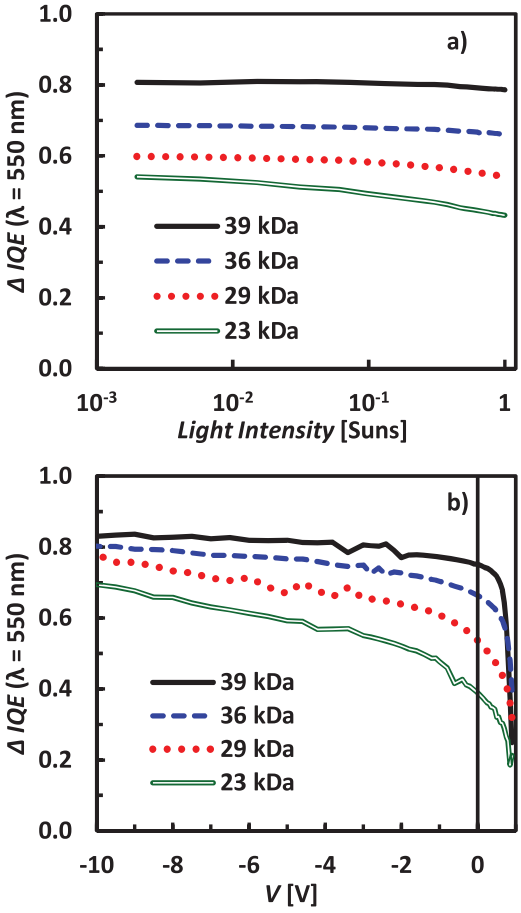

Figure 8. a) Internal quantum efficiency (λ = 550 nm) vs. light intensity and b) internal quantum efficiency (λ = 550 nm) vs. applied electrical bias (with a one sun light intensity white-light bias) for PBDTTPD BHJ solar cells processed in chlorobenzene.

The average IQE for all the photons absorbed by the device at a given light intensity, I', is calculated using Equation (2).

$$\mathrm{IQE}(I) = \frac{1}{I}\int_0^I \Delta\mathrm{IQE}(I')\mathrm{d}I' \tag{2}$$

By comparing the IQE at light intensity $I = I'$ to the IQE at low light intensity, the amount of recombination loss due to bimolecular recombination can be estimated. We find that at one sun light intensity (at J_{SC}) bimolecular recombination accounts for ≈1.8, ≈2.7, ≈6.5, and ≈15% of the recombination losses in 39, 36, 29, and 23 kDa PBDTTPD devices, respectively. Thus, bimolecular recombination losses are most significant in low M_n devices and contribute to the poor performance of these devices. These recombination losses, however, only account for a portion of the total difference in IQE between high and low M_n PBDTTPD devices since the IQE of low M_n devices is still significantly lower than that of high M_n devices at low light intensities where the rate of bimolecular recombination is low.

Geminate recombination, or the recombination of coulombically bound electron-hole pairs formed after charge transfer at polymer-fullerene heterojunctions, is another loss mechanism that can limit the efficiency of BHJ solar cells. The rate of geminate recombination can depend on the internal electric field in a device, which may give rise to bias-dependent photocurrent generation in devices that suffer from significant amounts of geminate recombination.[74–77] We measured the ΔIQE of PBDTTPD BHJ solar cells as a function of applied bias to probe the effects of geminate recombination and found that the ΔIQE of low M_n devices is significantly more bias-dependent than that of high M_n devices (Figure 8b). Specifically, the ΔIQE of 23 and 29 kDa devices increases by ≈78 and ≈45%, respectively, when a −10 V bias is applied to the devices (compared to the ΔIQE at J_{SC}), while the ΔIQE of 36 and 39 kDa devices only increases by ≈21 and ≈10%, respectively. Additionally, the current in the J–V curves (in the 3rd and 4th quadrants) of low M_n PBDTTPD devices processed in CN alone is more sloped than the current in high M_n devices, which also indicates that the photocurrent in low M_n devices is the most bias-dependent (Figure 2a). It should be noted that a portion of the increase in ΔIQE in reverse bias is likely due to free carrier generation in the large $PC_{70}BM$-rich domains in low M_n devices and not due to a decrease in geminate recombination.[78] That said, we hypothesize that geminate recombination losses do contribute to the poor performance of low M_n PBDTTPD devices; we note, however, that further investigation would be needed to quantify the amount of geminate recombination in these devices.

We hypothesize that the increased recombination loss in low M_n PBDTTPD devices is caused by the extensive phase separation in these BHJs, which increases the distance between the $PC_{70}BM$-rich domains and potentially decreases the amount of fullerene in the amorphous, mixed regions of these BHJs. We previously showed that isolated fullerene molecules in the amorphous, mixed regions of PBDTTPD BHJs can act as electron traps when the concentration of fullerene in these regions is below the percolation threshold for electron transport (<20 wt% fullerene).[50] This mechanism results in a bias-independent decrease in IQE because a fraction of the photogenerated charge-carriers are lost at these morphological traps. Vakhshouri et al.[79] demonstrated that when the concentration of fullerene in the mixed regions of polymer-fullerene BHJs is above the percolation threshold for electron transport, the electron mobility is highly sensitive to the fullerene concentration, increasing from ≈10^{-6} to ≈10^{-3} cm^2 V s^{-1} when the fullerene concentration is raised from ≈20 to ≈60 wt%, respectively. As a result, electron extraction through a percolated mixed region with relatively low fullerene content is slow and can be assisted with a strong electric field. Because low M_n PBDTTPD and $PC_{70}BM$ undergo extensive phase separation during spin-casting, a substantial portion of the $PC_{70}BM$ may reside in the large $PC_{70}BM$-rich domains in low M_n PBDTTPD BHJs, and the residual concentration of $PC_{70}BM$ mixed in the amorphous portions of low M_n PBDTTPD may be relatively low. We believe that the bias-dependent IQE in low M_n BHJs is an indication that the mixed regions in these BHJs have insufficient fullerene content for efficient electron transport without the aid of a strong electric field. Moreover, Maturová et al.[80] demonstrated that polymer-fullerene BHJ solar cells exhibit bias-dependent IQE and enhanced rates of bimolecular recombination when electrons must travel long distances through mixed regions in order to reach fullerene-rich domains (which have high electron mobility). Electrons generated in the mixed regions of low M_n

PBDTTPD BHJs must travel relatively far to reach $PC_{70}BM$-rich domains because the large $PC_{70}BM$-rich domains in these BHJs are spaced further apart than the smaller $PC_{70}BM$-rich domains in high M_n PBDTTPD BHJs. Additionally, holes generated in the large fullerene-rich domains in low M_n BHJs must travel long distances through the fullerene-rich domains in order to reach pure PBDTTPD domains.

Furthermore, Jamieson et al.[81] recently reported that the electron affinity of aggregated $PC_{60}BM$ is larger (i.e., lower-lying lowest occupied molecular orbital vs. vacuum) than the electron affinity of $PC_{60}BM$ molecules intimately mixed with polymers. Due to this energetic difference, there may be a driving force for electrons to move from the mixed regions of polymer-fullerene BHJs to the fullerene-rich domains, which have high electron mobility. It was hypothesized that this energetic driving force spatially separates coulombically bound electron-hole pairs and decreases the rate of geminate recombination in polymer-fullerene BHJs. Thus, a large amount of interfacial area between the amorphous, mixed regions and fullerene-rich domains in polymer-fullerene BHJs may be beneficial for charge-generation. We hypothesize that the rate of geminate recombination in low M_n PBDTTPD BHJ solar cells may be increased to some extent because the large fullerene-rich domains in these BHJs provide relatively little interfacial area between the fullerene-rich domains and the other phases in these BHJs.

3. Conclusions

Low M_n PBDTTPD BHJ solar cells perform poorly because low M_n PBDTTPD and $PC_{70}BM$ phase separate extensively during spin-casting, forming large (≈300–400 nm in diameter) $PC_{70}BM$-rich domains. These large domains increase the amount of charge-carrier recombination in low M_n devices, but do not significantly affect the exciton splitting efficiency. Increasing the M_n of PBDTTPD substantially improves device performance by decreasing the size of the $PC_{70}BM$-rich domains in these BHJs. High M_n PBDTTPD may quickly form a fibrillar polymer network during spin-casting because it has a low solubility, and this fibrillar network may act as a template for phase separation, which prevents large $PC_{70}BM$-rich domains from forming in these BHJs. Thus, high M_n PBDTTPD provides superior solar cell performance because of its propensity to self-assemble in solution. Additionally, the IQE of PBDTTPD devices can be significantly enhanced through the use of the solvent additive CN. This additive likely prevents large $PC_{70}BM$-rich domains from forming in low M_n PBDTTPD BHJs by inducing PBDTTPD to form a fibrillar polymer network in solution while the $PC_{70}BM$ is still solubilized. These results shed light on the mechanism that causes the strong correlation between the M_n of PBDTTPD and BHJ solar cell performance and demonstrates that solvent additives can be used to improve the performance of devices made with lower M_n PBDTTPD.

Because the BHJ solar cell performance of a variety of other D-A polymers depends on M_n[13–26] and because many D-A polymers are processed with solvent additives,[21,31–33,35–45] we expect that these findings can be extended to a variety of D-A polymer-fullerene systems. Thus, the insight gained from this study may expedite the process of optimizing the BHJ morphology and solar cell performance of D-A polymers designed and synthesized in the future.

4. Experimental Section

Solar Cell Preparation: Glass substrates patterned with ITO (15 Ω/□, Xinyan Technologies LTD.) were scrubbed with dilute Extran 300 detergent and ultrasonicated in a dilute Extran 300 detergent solution for 15 min. The substrates were then rinsed with deionized (DI) water for 5 min, sequentially ultrasonicated in acetone and isopropyl alcohol baths for 15 min, and rinsed in DI water for 5 min. The substrates were dried with nitrogen gas, placed in an oven (≈115 °C) for 30 min, and then exposed to a UV-ozone plasma for 15 min. An aqueous solution of PEDOT:PSS (Clevios P VP AI 4083) was spin-cast onto the substrates at 4,500 rpm, and the substrates were thermally annealed at 140 °C for 10 min. The substrates were then transferred to a dry nitrogen glovebox (<5 ppm O_2). All solutions were prepared in the glovebox using PBDTTPD synthesized as described in the Supporting Information, $PC_{70}BM$ purchased from Solenne BV, and chlorobenzene and 1-chloronaphthalene purchased from Sigma-Aldrich. Solutions were dissolved overnight at 115 °C, and active layers were spin-cast at 1200–1500 rpm for 45 s (500 rpm s^{-1}) from 115 °C solutions with concentrations between 17.5 and 20 mg total solids mL^{-1}. The active layer thickness was independently optimized for each batch of PBDTTPD (all optimized with thickness between 80 and 120 nm). Calcium (7 nm thick, Plasmaterials) and aluminium (150 nm thick, K. J. Lesker) electrodes were thermally evaporated (≈1×10^{-7} torr) through a shadow mask, which defined the device active area to 0.1 cm^2. Device active layer thicknesses were measured with a Veeco Dektak profilometer.

Solar Cell Characterization: Current–voltage measurements were performed in a dry nitrogen glovebox using a Keithley 2400 source meter and a Spectra-Physics 91160–1000 solar simulator (calibrated to one sun, AM1.5 G, with a NREL certified KG-5 filtered silicon photodiode). EQE measurements were performed with a Stanford Research Systems model SR830 DSP lock-in amplifier and a white-light bias supplied by a LED array (intensity calibrated with a KG-5 photodiode). IQE measurements were performed using the method developed by Burkhard et al.[82]

Transmission Electron Microscopy: The active layers of PBDTTPD BHJ solar cells (from the area between metal electrodes) were floated off the substrate by dissolving the PEDOT:PSS with DI water, and the films were collected onto lacey carbon-coated TEM grids (Electron Microscopy Sciences). TEM images were recorded in bright-field mode with an accelerating voltage of 120 keV using a FEI Tecnai BioTWIN transmission electron microscope equipped with a FEI 4000 × 4000 eagle CCD camera. A 100 μm objective aperture and –10 μm defocus were used to attain optimal image contrast and resolution.

X-Ray Diffraction: Active layers were spin-cast onto PEDOT:PSS-covered silicon substrates. GIXD experiments were carried out at the Stanford Synchrotron Radiation Laboratory (SSRL) beamline 11–3 using a X-ray energy of 12.7 keV, a MAR 345 image plate area detector, a helium-filled sample chamber, and an incident X-ray beam angle of ≈0.12 °. Local specular scans for the pole figures were taken with an incident X-ray beam angle of ≈7.7 ± 0.5 °. SAXS experiments were carried out at the SSRL beamline 4–2 with an X-ray energy of 14 keV, a sample to detector distance of 3.5 m, and a Rayonix MX225-HE CCD detector. Solutions were contained in 1 mm diameter quartz capillary tubes (purchased from The Charles Supper Company). USAXS experiments were carried out at the Argonne National Laboratory Advanced Photon Source 15-ID USAXS instrument, which employs Bonse-Hart-type double-crystal optics.[83] Measurements were performed in a transmission geometry using collimated and monochromatic X-rays with an energy of 16.9 keV (2 × 0.8 mm beam size). The data was collected in slit-smeared geometry and numerically desmeared to recover pinhole-collimated data.[83] The SAXS and USAXS data was stitched and fit using the Igor data analysis package written by Dr. Jan Ilavsky.

UV-Vis Absorption: Absorption measurements were performed with an Ocean Optics DT-1000-CE UV-Vis spectrometer and 1 mm path length quartz cuvettes. Before acquiring the absorption data, the solutions were heated to ≈115 °C and absorption spectra were acquired sequentially as the solutions cooled to room temperature.

Molecular Weight Characterization: Polymer solutions (1 mg mL^{-1}) were prepared using HPLC grade chloroform. Samples were briefly heated and then allowed to return to room temperature prior to filtering through a 0.45 μm PTFE filter. Size exclusion chromatography (Waters 2695 Separation Module and a Waters 486 Tunable Absorption Detector) was performed with HPLC grade chloroform at an elution rate of at 1.0 mL min^{-1} through three PLgel Mixed-C columns. The particle size in the columns was 5 μm and the columns were maintained at room temperature. The apparent molecular weight and polydispersity (M_w/M_n) were determined with a calibration based on linear polystyrene standards using Millennium software from Waters.

Supporting Information

Supporting Information is available from the Wiley Online Library or from the author.

Acknowledgements

The authors acknowledge Eric Hoke and Sean Sweetnam for helpful discussion and thank the Advanced Imaging and Characterization Laboratories at King Abdullah University of Science and Technology (KAUST) for technical support. This publication was based on work supported by the Center for Advanced Molecular Photovoltaics (CAMP) (Award No KUS-C1–015–21), made possible by KAUST. J.A.B. acknowledges government support by the Department of Defense (DoD) through the National Defense Science & Engineering Graduate Fellowship (NDSEG) Program, and P.M.B. and A.E.L. acknowledge financial support under Baseline Research Funding from KAUST. Portions of this research were carried out at the Stanford Synchrotron Radiation Lightsource, a Directorate of SLAC National Accelerator Laboratory and an Office of Science User Facility operated for the U.S. Department of Energy Office of Science by Stanford University. The beamline 4–2 is part of the SSRL Structural Molecular Biology Program which is supported by the DOE Office of Biological and Environmental Research, and by the National Institutes of Health, National Institute of General Medical Sciences (including P41GM103393) and the National Center for Research Resources (P41RR001209). The contents of this publication are solely the responsibility of the authors and do not necessarily represent the official views of NIGMS, NCRR or NIH. ChemMatCARS Sector 15 is principally supported by the National Science Foundation/Department of Energy under grant number NSF/CHE-0822838. Use of the Advanced Photon Source was supported by the U. S. Department of Energy, Office of Science, Office of Basic Energy Sciences, under Contract No. DE-AC02–06CH11357.

Received: November 11, 2013
Revised: January 30, 2014
Published online: March 20, 2014

[1] G. Yu, J. Gao, J. C. Hummelen, F. Wudl, A. J. Heeger, *Science* **1995**, *270*, 1789.
[2] Z. He, C. Zhong, S. Su, M. Xu, H. Wu, Y. Cao, *Nat. Photonics* **2012**, *6*, 591.
[3] J. You, L. Dou, K. Yoshimura, T. Kato, K. Ohya, T. Moriarty, K. Emery, C.-C. Chen, J. Gao, G. Li, Y. Yang, *Nat. Commun.* **2013**, *4*, 1446.
[4] E. E. Havinga, W. ten Hoeve, H. Wynberg, *Synth. Met.* **1993**, *57*, 299.
[5] C. J. Brabec, S. Gowrisanker, J. J. M. Halls, D. Laird, S. Jia, S. P. Williams, *Adv. Mater.* **2010**, *22*, 3839.
[6] L. Dou, J. You, J. Yang, C. Chen, Y. He, S. Murase, T. Moriarty, K. Emery, G. Li, Y. Yang, *Nat. Photonics* **2012**, *6*, 180.
[7] Y. Li, *Acc. Chem. Res.* **2012**, *45*, 723.
[8] G. Li, R. Zhu, Y. Yang, *Nat. Photonics* **2012**, *6*, 153.
[9] R. S. Kularatne, H. D. Magurudeniya, P. Sista, M. C. Biewer, M. C. Stefan, *J. Polym. Sci. Part A Polym. Chem.* **2013**, *51*, 743.
[10] C. Risko, M. D. McGehee, J.-L. Brédas, *Chem. Sci.* **2011**, *2*, 1200.
[11] P. M. Beaujuge, J. M. J. Fréchet, *J. Am. Chem. Soc.* **2011**, *133*, 20009.
[12] Z. B. Henson, K. Müllen, G. C. Bazan, *Nat. Chem.* **2012**, *4*, 699.
[13] R. C. Coffin, J. Peet, J. Rogers, G. C. Bazan, *Nat. Chem.* **2009**, *1*, 657.
[14] D. J. D. Moet, M. Lenes, J. D. Kotlarski, S. C. Veenstra, J. Sweelssen, M. M. Koetse, B. de Boer, P. W. M. Blom, *Org. Electron.* **2009**, *10*, 1275.
[15] S. Wakim, S. Beaupré, N. Blouin, B.-R. Aich, S. Rodman, R. Gaudiana, Y. Tao, M. Leclerc, *J. Mater. Chem.* **2009**, *19*, 5351.
[16] J. C. Bijleveld, A. P. Zoombelt, S. G. J. Mathijssen, M. M. Wienk, M. Turbiez, D. M. de Leeuw, R. A. J. Janssen, *J. Am. Chem. Soc.* **2009**, *131*, 16616.
[17] M. Tong, S. Cho, J. T. Rogers, K. Schmidt, B. B.Y. Hsu, D. Moses, R. C. Coffin, E. J. Kramer, G. C. Bazan, A. J. Heeger, *Adv. Funct. Mater.* **2010**, *20*, 3959.
[18] C. Müller, E. Wang, L. M. Andersson, K. Tvingstedt, Y. Zhou, M. R. Andersson, O. Inganäs, *Adv. Funct. Mater.* **2010**, *20*, 2124.
[19] J.-H. Huang, F.-C. Chen, C.-L. Chen, A. T. Huang, Y.-S. Hsiao, C.-M. Teng, F.-W. Yen, P. Chen, C.-W. Chu, *Org. Electron.* **2011**, *12*, 1755.
[20] I. Osaka, M. Saito, H. Mori, T. Koganezawa, K. Takimiya, *Adv. Mater.* **2011**, *24*, 425.
[21] T.-Y. Chu, J. Lu, S. Beaupré, Y. Zhang, J.-R. Pouliot, J. Zhou, A. Najari, M. Leclerc, Y. Tao, *Adv. Funct. Mater.* **2012**, *22*, 2345.
[22] X. Zhao, H. Tang, D. Yang, H. Li, W. Xu, L. Yin, X. Yang, *Chinese J. Chem.* **2012**, *30*, 2052.
[23] B. R. Aïch, J. Lu, S. Beaupré, M. Leclerc, Y. Tao, *Org. Electron.* **2012**, *13*, 1736.
[24] W. Li, W. S. C. Roelofs, M. M. Wienk, R. A. J. Janssen, *J. Am. Chem. Soc.* **2012**, *134*, 13787.
[25] W. Li, K. H. Hendriks, W. S. C. Roelofs, Y. Kim, M. M. Wienk, R. A. J. Janssen, *Adv. Mater.* **2013**, *25*, 3182.
[26] K. H. Hendriks, G. H. L. Heintges, V. S. Gevaerts, M. M. Wienk, R. A. J. Janssen, *Angew. Chemie Int. Ed.* **2013**, *52*, 8341.
[27] C. Piliego, T. W. Holcombe, J. D. Douglas, C. H. Woo, P. M. Beaujuge, J. M. J. Fréchet, *J. Am. Chem. Soc.* **2010**, *132*, 7595.
[28] Y. Zhang, S. K. Hau, H.-L. Yip, Y. Sun, O. Acton, A. K.-Y. Jen, *Chem. Mater.* **2010**, *22*, 2696.
[29] Y. Zou, A. Najari, P. Berrouard, S. Beaupré, B.-R. Aich, Y. Tao, M. Leclerc, *J. Am. Chem. Soc.* **2010**, *132*, 5330.
[30] C. Cabanetos, A. El Labban, J. A. Bartelt, J. D. Douglas, W. R. Mateker, J. M. J. Fréchet, M. D. McGehee, P. M. Beaujuge, *J. Am. Chem. Soc.* **2013**, *135*, 4656.
[31] J. Peet, J. Y. Kim, N. E. Coates, W. L. Ma, D. Moses, A. J. Heeger, G. C. Bazan, *Nat. Mater.* **2007**, *6*, 497.
[32] J. K. Lee, W. L. Ma, C. J. Brabec, J. D. Yuen, J. S. Moon, J. Y. Kim, K. Lee, G. C. Bazan, A. J. Heeger, *J. Am. Chem. Soc.* **2008**, *130*, 3619.
[33] H.-Y. Chen, J. Hou, S. Zhang, Y. Liang, G. Yang, Y. Yang, L. Yu, Y. Wu, G. Li, *Nat. Photonics* **2009**, *3*, 649.
[34] C. H. Woo, P. M. Beaujuge, T. W. Holcombe, O. P. Lee, J. M. J. Fréchet, *J. Am. Chem. Soc.* **2010**, *132*, 15547.
[35] C. V. Hoven, X.-D. Dang, R. C. Coffin, J. Peet, T.-Q. Nguyen, G. C. Bazan, *Adv. Mater.* **2010**, *22*, E63.
[36] J. S. Moon, C. J. Takacs, S. Cho, R. C. Coffin, H. Kim, G. C. Bazan, A. J. Heeger, *Nano Lett.* **2010**, *10*, 4005.
[37] Y. Liang, Z. Xu, J. Xia, S.-T. Tsai, Y. Wu, G. Li, C. Ray, L. Yu, *Adv. Mater.* **2010**, *22*, E135.

[38] J. C. Bijleveld, V. S. Gevaerts, D. Di Nuzzo, M. Turbiez, S. G. J. Mathijssen, D. M. de Leeuw, M. M. Wienk, R. A. J. Janssen, *Adv. Mater.* **2010**, *22*, E242.
[39] M. R. Hammond, R. J. Kline, A. A. Herzing, L. J. Richter, D. S. Germack, H.-W. Ro, C. L. Soles, D. A. Fischer, T. Xu, L. Yu, M. F. Toney, D. M. Delongchamp, *ACS Nano* **2011**, *5*, 8248.
[40] C. M. Amb, S. Chen, K. R. Graham, J. Subbiah, C. E. Small, F. So, J. R. Reynolds, *J. Am. Chem. Soc.* **2011**, *133*, 10062.
[41] J. T. Rogers, K. Schmidt, M. F. Toney, E. J. Kramer, G. C. Bazan, *Adv. Mater.* **2011**, *23*, 2284.
[42] Y. Gu, C. Wang, T. P. Russell, *Adv. Energy Mater.* **2012**, *2*, 683.
[43] F. Liu, Y. Gu, C. Wang, W. Zhao, D. Chen, A. L. Briseno, T. P. Russell, *Adv. Mater.* **2012**, *24*, 3947.
[44] K. R. Graham, P. M. Wieruszewski, R. Stalder, M. J. Hartel, J. Mei, F. So, J. R. Reynolds, *Adv. Funct. Mater.* **2012**, *22*, 4801.
[45] B. A. Collins, Z. Li, J. R. Tumbleston, E. Gann, C. R. McNeill, H. Ade, *Adv. Energy Mater.* **2013**, *3*, 65.
[46] K. Schmidt, C. J. Tassone, J. R. Niskala, A. T. Yiu, O. P. Lee, T. M. Weiss, C. Wang, J. M. J. Fréchet, P. M. Beaujuge, M. F. Toney, *Adv. Mater.* **2014**, *26*, 300.
[47] E. T. Hoke, K. Vandewal, J. A. Bartelt, W. R. Mateker, J. D. Douglas, R. Noriega, K. R. Graham, J. M. J. Fréchet, A. Salleo, M. D. McGehee, *Adv. Energy Mater.* **2013**, *3*, 220.
[48] Z. M. Beiley, M. D. McGehee, *Energy Environ. Sci.* **2012**, *5*, 9173.
[49] V. S. Gevaerts, A. Furlan, M. M. Wienk, M. Turbiez, R. A. J. Janssen, *Adv. Mater.* **2012**, *24*, 2130.
[50] J. A. Bartelt, Z. M. Beiley, E. T. Hoke, W. R. Mateker, J. D. Douglas, B. A. Collins, J. R. Tumbleston, K. R. Graham, A. Amassian, H. Ade, J. M. J. Fréchet, M. F. Toney, M. D. McGehee, *Adv. Energy Mater.* **2013**, *3*, 364.
[51] D. R. Kozub, K. Vakhshouri, L. M. Orme, C. Wang, A. Hexemer, E. D. Gomez, *Macromolecules* **2011**, *44*, 5722.
[52] D. Chen, A. Nakahara, D. Wei, D. Nordlund, T. P. Russell, *Nano Lett.* **2011**, *11*, 561.
[53] D. Chen, F. Liu, C. Wang, A. Nakahara, T. P. Russell, *Nano Lett.* **2011**, *11*, 2071.
[54] N. D. Treat, M. A. Brady, G. Smith, M. F. Toney, E. J. Kramer, C. J. Hawker, M. L. Chabinyc, *Adv. Energy Mater.* **2011**, *1*, 82.
[55] R. J. Kline, M. D. McGehee, E. N. Kadnikova, J. Liu, J. M. J. Fréchet, M. F. Toney, *Macromolecules* **2005**, *38*, 3312.
[56] D. T. Duong, M. F. Toney, A. Salleo, *Phys. Rev. B* **2012**, *86*, 205205.
[57] J. L. Baker, L. H. Jimison, S. Mannsfeld, S. Volkman, S. Yin, V. Subramanian, A. Salleo, A. P. Alivisatos, M. F. Toney, *Langmuir* **2010**, *26*, 9146.
[58] J. Rivnay, S. C. B. Mannsfeld, C. E. Miller, A. Salleo, M. F. Toney, *Chem. Rev.* **2012**, *112*, 5488.
[59] J. Rivnay, R. Steyrleuthner, L. H. Jimison, A. Casadei, Z. Chen, M. F. Toney, A. Facchetti, D. Neher, A. Salleo, *Macromolecules* **2011**, *44*, 5246.
[60] R. Steyrleuthner, M. Schubert, I. Howard, B. Klaumünzer, K. Schilling, Z. Chen, P. Saalfrank, F. Laquai, A. Facchetti, D. Neher, *J. Am. Chem. Soc.* **2012**, *134*, 18303.
[61] G. Beaucage, *J. Appl. Crystallogr.* **1995**, *28*, 717.
[62] G. Beaucage, *J. Appl. Crystallogr.* **1996**, *29*, 134.
[63] B. Hammouda, *J. Appl. Crystallogr.* **2010**, *43*, 716.
[64] R. J. Roe, *Methods X-Ray Scattering: Neutron Scattering Polymer Science*, Oxford University Press Inc., New York, USA **2000**
[65] V. O. Glatter, O. Kratky, *Small Angle X-Ray Scattering*, Academic Press Inc., New York, USA **1982**.
[66] There was an insufficient amount of 39 kDa PBDTTPD remaining when this experiment was performed, so 41 kDa PBDTTPD (PDI = 1.8) was used as a replacement. The 39 and 41 kDa PBDTTPD had very similar device performance and GIXD scattering profiles.
[67] M. Knaapila, V. M. Garamus, F. B. Dias, L. Almásy, F. Galbrecht, A. Charas, J. Morgado, H. D. Burrows, U. Scherf, A. P. Monkman, *Macromolecules* **2006**, *39*, 6505.
[68] M. Rubinstein, R. H. Colby, *Polymer Physics*, Oxford University Press Inc., New York, USA **2003**.
[69] N. Shin, L. J. Richter, A. A. Herzing, R. J. Kline, D. M. DeLongchamp, *Adv. Energy Mater.* **2013**, *3*, 938.
[70] T.-Y. Chu, S. Alem, S.-W. Tsang, S.-C. Tse, S. Wakim, J. Lu, G. Dennler, D. Waller, R. Gaudiana, Y. Tao, *Appl. Phys. Lett.* **2011**, *98*, 253301.
[71] G. F. Burkhard, E. T. Hoke, S. R. Scully, M. D. McGehee, *Nano Lett.* **2009**, *9*, 4037.
[72] D. R. Haynes, A. Tokmakoff, S. M. George, *Chem. Phys. Lett.* **1993**, *214*, 50.
[73] B. Fischer, M. Keil, P. Fath, E. Bucher, *Part Photovolt. Spec. Conf. 2002. Conf. Rec. Twenty-Ninth IEEE* New Orleans.
[74] V. Mihailetchi, L. Koster, J. Hummelen, P. W. M. Blom, *Phys. Rev. Lett.* **2004**, *93*, 216601.
[75] R. A. Marsh, J. M. Hodgkiss, R. H. Friend, *Adv. Mater.* **2010**, *22*, 3672.
[76] K. Tvingstedt, K. Vandewal, F. Zhang, O. Inganäs, *J. Phys. Chem. C* **2010**, *114*, 21824.
[77] S. Albrecht, W. Schindler, J. Kurpiers, J. Kniepert, J. C. Blakesley, I. Dumsch, S. Allard, K. Fostiropoulos, U. Scherf, D. Neher, *J. Phys. Chem. Lett.* **2012**, *3*, 640.
[78] G. F. Burkhard, E. T. Hoke, Z. M. Beiley, M. D. McGehee, *J. Phys. Chem. C* **2012**, *116*, 26674.
[79] K. Vakhshouri, D. R. Kozub, C. Wang, A. Salleo, E. D. Gomez, *Phys. Rev. Lett.* **2012**, *108*, 026601.
[80] K. Maturová, S. S. van Bavel, M. M. Wienk, R. A. J. Janssen, M. Kemerink, *Nano Lett.* **2009**, *9*, 3032.
[81] F. C. Jamieson, E. B. Domingo, T. McCarthy-Ward, M. Heeney, N. Stingelin, J. R. Durrant, *Chem. Sci.* **2012**, *3*, 485.
[82] G. F. Burkhard, E. T. Hoke, M. D. McGehee, *Adv. Mater.* **2010**, *22*, 3293.
[83] J. Ilavsky, P. R. Jemian, A. J. Allen, F. Zhang, L. E. Levine, G. G. Long, *J. Appl. Crystallogr.* **2009**, *42*, 469.

